Supplementary Information

Charge-engineered cellulose nanofibril binders for PFAS-free, high-loading lithium battery positive electrodes

Sang-Woo Kim[1†], Nag-Young Kim[2†], Anseong Park[3], Jinho Ha[4], Cheol Bak[2], Yoojin Kim[2], Seong-Seok Chae[2], Jung-Hui Kim[2], Sang-Cheol Nam[5], Chaoji Chen[6], Yong Min Lee[2,4], Jung-Il Choi[4,7], Won Bo Lee[3*], and Sang-Young Lee[2,4*]

[1]Department of Energy and Chemical Engineering, Ulsan National Institute of Science and Technology (UNIST), Ulsan, 44919, Republic of Korea

[2]Department of Chemical and Biomolecular Engineering, Yonsei University, Seoul, 03772, Republic of Korea

[3]School of Chemical and Biological Engineering, Institute of Chemical Processes, Seoul National University, Seoul, Republic of Korea

[4]Department of Battery Engineering, Yonsei University, Seoul, 03772, Republic of Korea

[5]Energy Materials Research Center, POSCO Future M, Sejong-si, 30002, Republic of Korea

[6]School of Resource and Environmental Sciences, Wuhan University, Wuhan, China

[7]School of Mathematics and Computing (Computational Science and Engineering), Yonsei University, Seoul, 03772, Republic of Korea

[†]These authors contributed equally to this work

✉email: wblee@snu.ac.kr; syleek@yonsei.ac.kr

Supplementary Figures

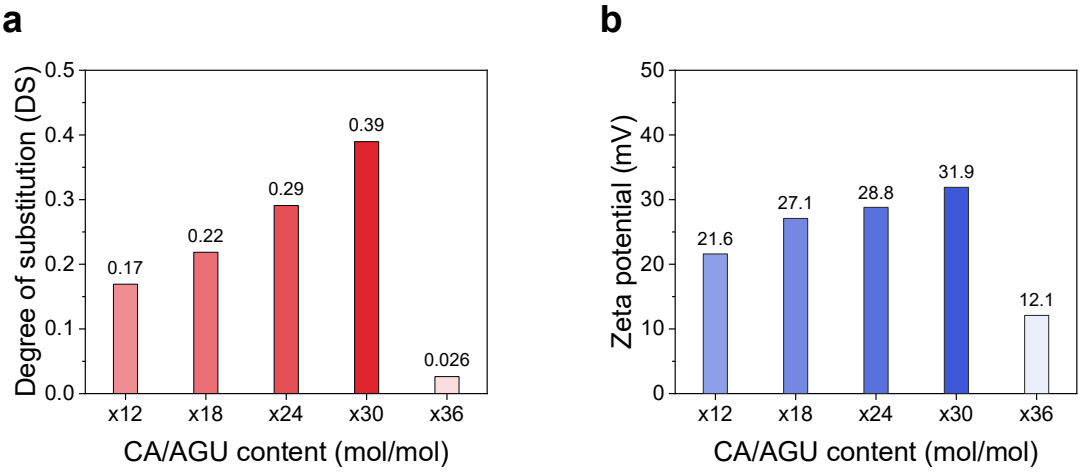

Supplementary Fig. 1 | Quantification of cationic functionalization in c-CNF. a, Degree of substitution (DS) as a function of the molar ratio of cationic agent (CA) to anhydroglucose unit (AGU). **b**, Apparent zeta potential of c-CNF dispersions as a function of CA/AGU ratio, indicating surface charge modulation via cationic functionalization.

The nitrogen content (N%) of c-CNF was determined using elemental analysis, and the DS was calculated using the following equation (1)[1]:

$$\text{Degree of substitution (DS)} = \frac{162 \cdot N\%}{14 - 151.5 \cdot N\%} \quad (1)$$

, where 162 is the molar mass of AGU, 14 is the atomic mass of nitrogen, and 151.5 corresponds to the molar mass of the cationic substituent group.

Supplementary Fig. 2 | Visual comparison of CNF suspensions. The c-CNF suspension exhibits more uniform dispersion and colloidal stability compared to other CNF suspensions.

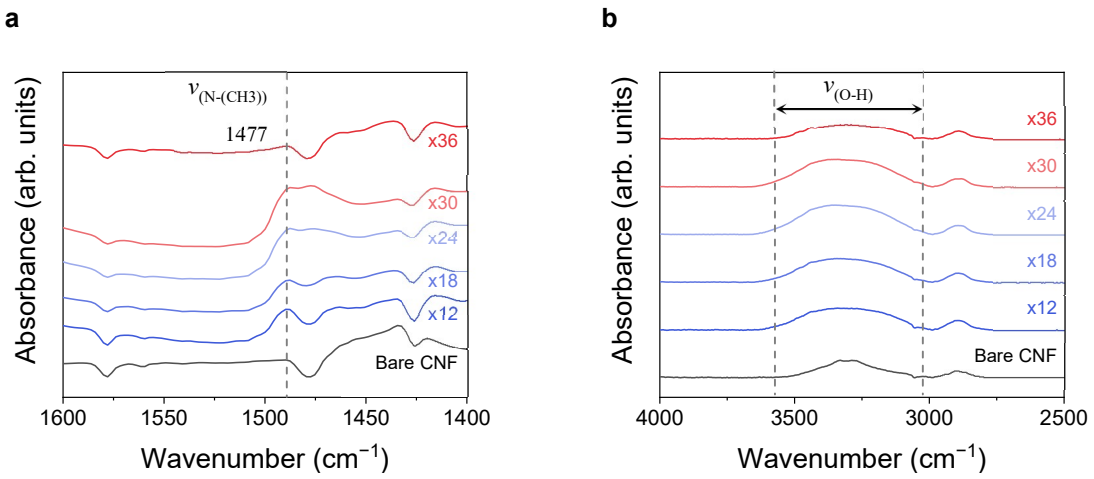

Supplementary Fig. 3 | FTIR spectra of CNFs prepared under various cationic agent concentrations. a, FTIR spectra highlighting the characteristic N–(CH_3) stretching peak at 1,477 cm^{-1}, indicating successful cationic functionalization. **b**, FTIR spectra showing broad O–H stretching region of cellulose, reflecting changes in hydrogen bonding with increasing degree of substitution.

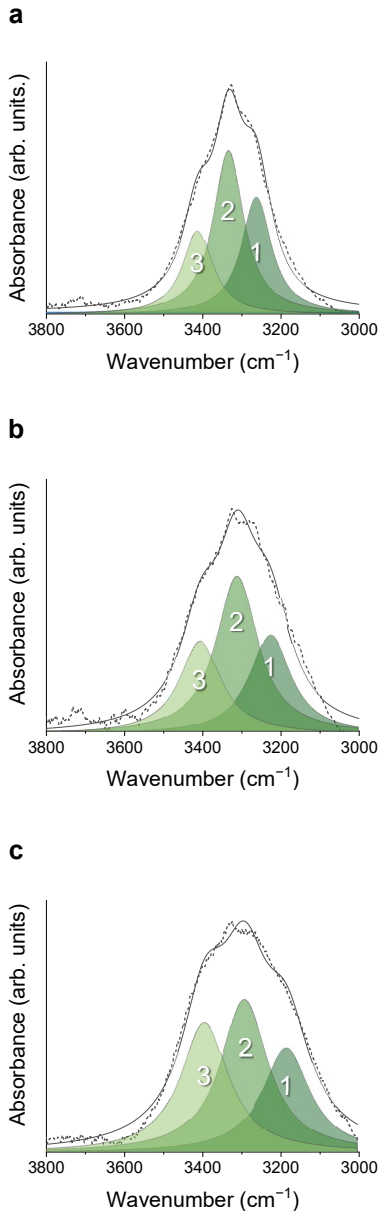

Supplementary Fig. 4 | FT–IR-based analysis of hydrogen bonding in CNFs. a–c, Second derivative FTIR spectra of b-CNF (**a**), a-CNF (**b**), and c-CNF (**c**). Three major bands are assigned to distinct hydrogen bonding interactions: O6–H···O3′ intermolecular H-bond (peak 1), O3–H···O5 intramolecular H-bond (peak 2), and O2–H···O6 intramolecular H-bond (peak 3), respectively[2].

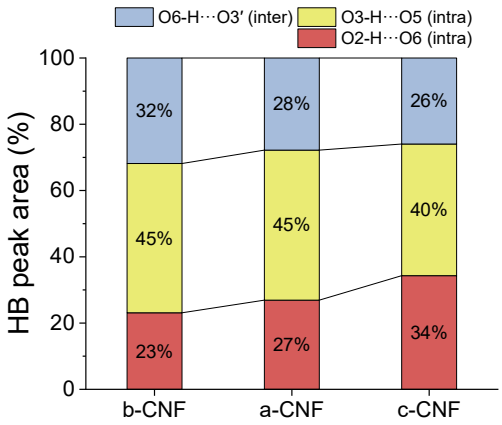

Supplementary Fig. 5 | Quantitative analysis of hydrogen bonding in CNFs based on FTIR spectra. Hydrogen bonding peak areas calculated from the deconvoluted FTIR spectra in the 3000–3600 cm^{-1} region, corresponding to O–H stretching vibrations.

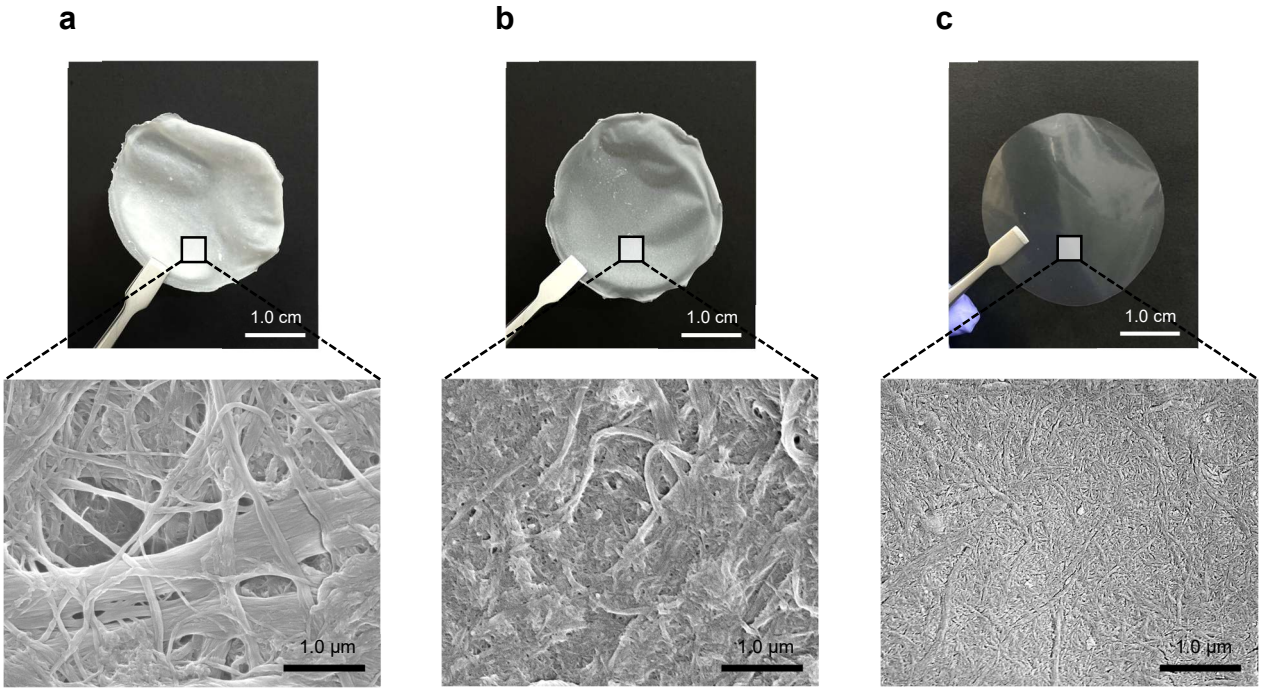

Supplementary Fig. 6 | Morphological comparison of cellulose films with different surface chemistries. a–c, Photographs of b-CNF (**a**), a-CNF (**b**), and c-CNF films (**c**). Corresponding SEM images show the distinct fiber morphologies of the three cellulose films, reflecting differences in surface functionalization and dispersion quality.

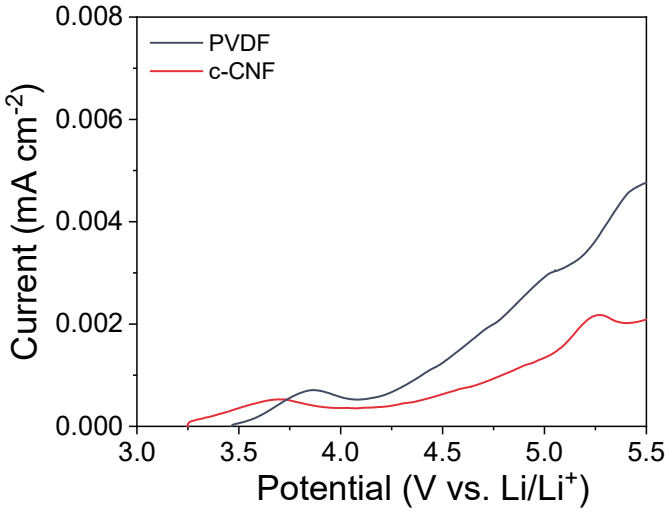

Supplementary Fig. 7 | Linear sweep voltammetry (LSV) profiles of PVDF and c-CNF binders. The measurements were conducted to evaluate the electrochemical stability of the binder films up to 5.5 V.

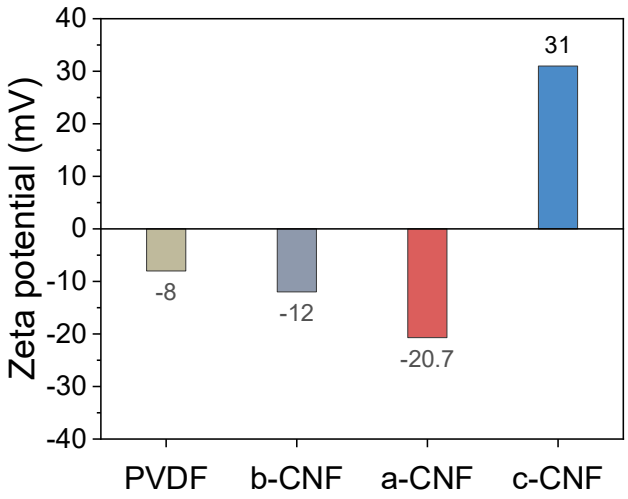

Supplementary Fig. 8 | Zeta potential analysis of binder dispersions with conductive additives. Zeta potential measurements reveal surface charge variations resulting from different binder functionalization, indicating their influence on colloidal stability.

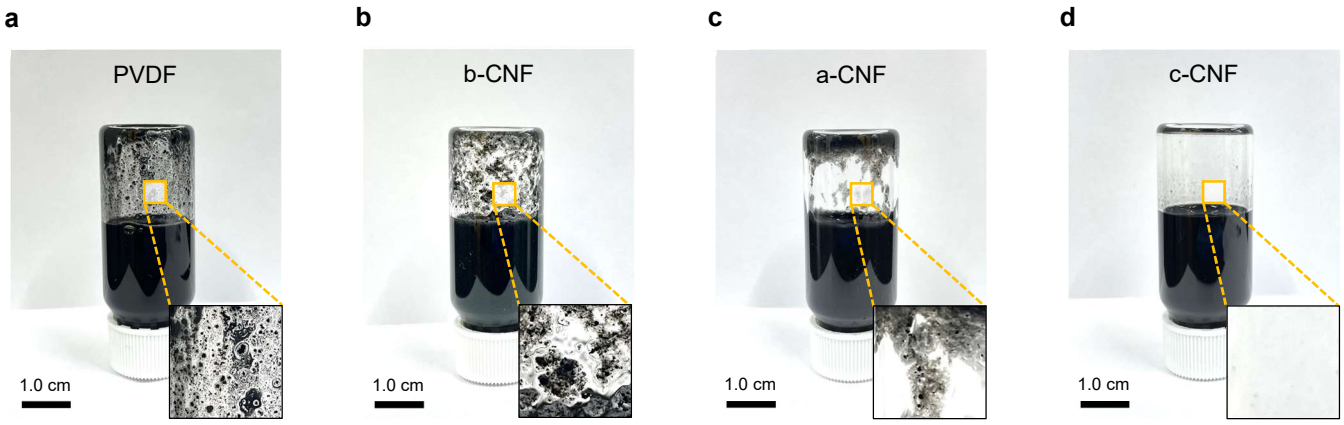

Supplementary Fig. 9 | Visual comparison of model slurries containing carbon black and different binders. a–d, Photographs of model slurries prepared with carbon black and PVDF (**a**), b-CNF (**b**), a-CNF (**c**), and c-CNF binders (**d**), highlighting differences in dispersion behavior depending on binder chemistry.

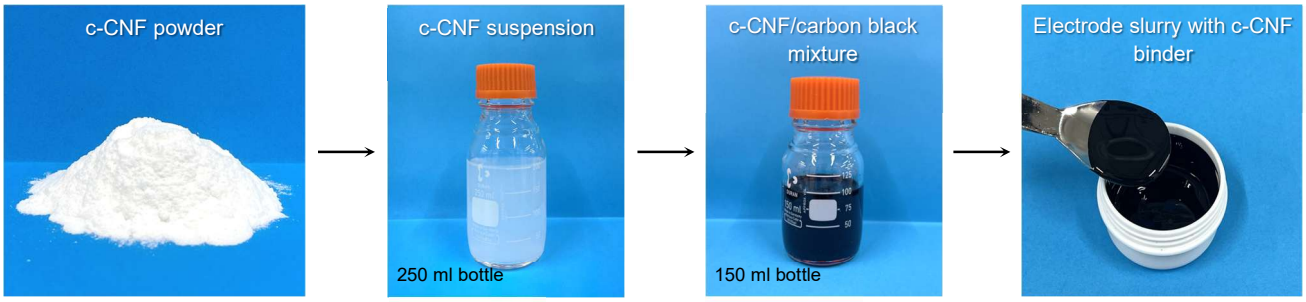

Supplementary Fig. 10 | Stepwise fabrication of electrode slurry using c-CNF binder. Digital photographs of the sequential process integrating c-CNF binder with carbon black additives and NCM811 positive active materials.

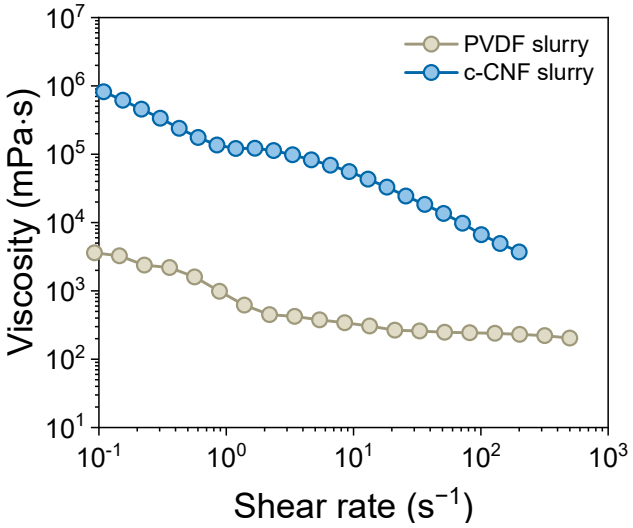

Supplementary Fig. 11 | Rheological behavior of electrode slurries with 76 wt% solid content. Apparent viscosity profiles as a function of shear rate, highlighting shear-thinning behavior of c-CNF slurry.

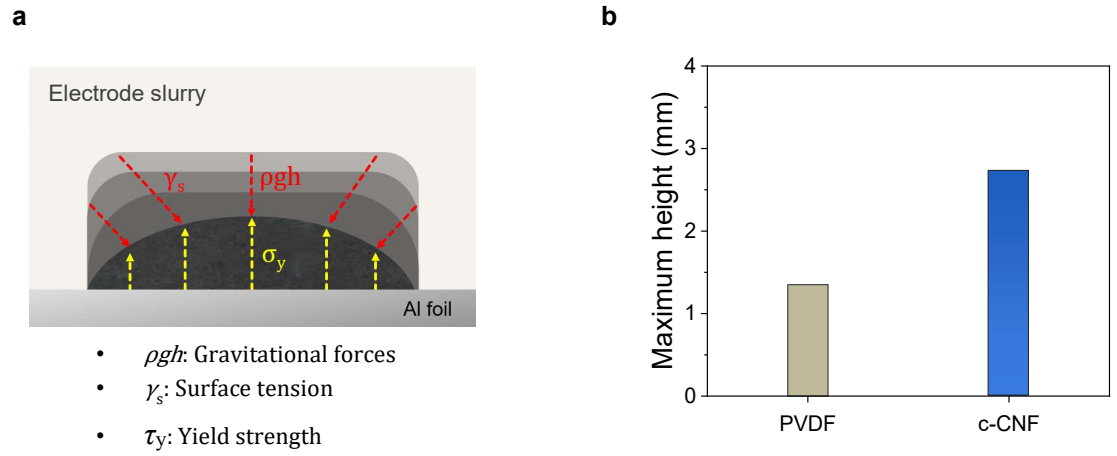

Supplementary Fig. 12 | Gravitational slumping behavior of electrode slurries. a, Frame superposition schematic illustrating time-dependent deformation of cast slurries. **b**, Maximum stable coating height (h_{max}) estimated using the following equation[3]:

$$h_{max} = \frac{\tau_y}{\rho g} \quad (2)$$

where τ_y, ρ, and g represent the yield strength, slurry density, and gravitational acceleration, respectively.

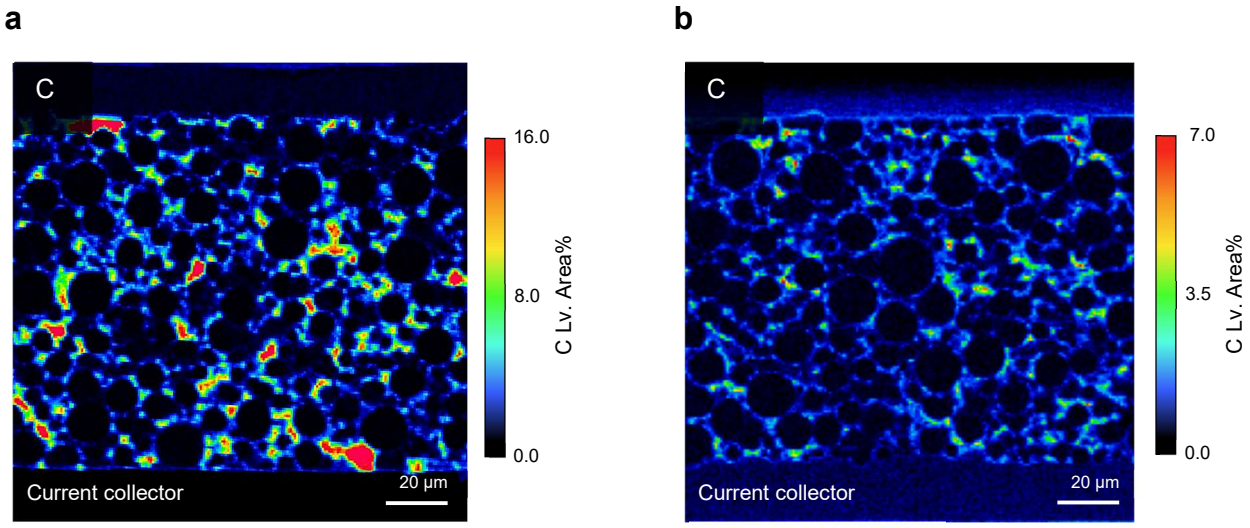

Supplementary Fig. 13 | Cross-sectional FE-EPMA mapping images of electrodes. a, PVDF electrode. **b**, c-CNF electrode. The mapping images show the distribution of carbon atoms within each binder matrix, highlighting differences in dispersion and interfacial morphology.

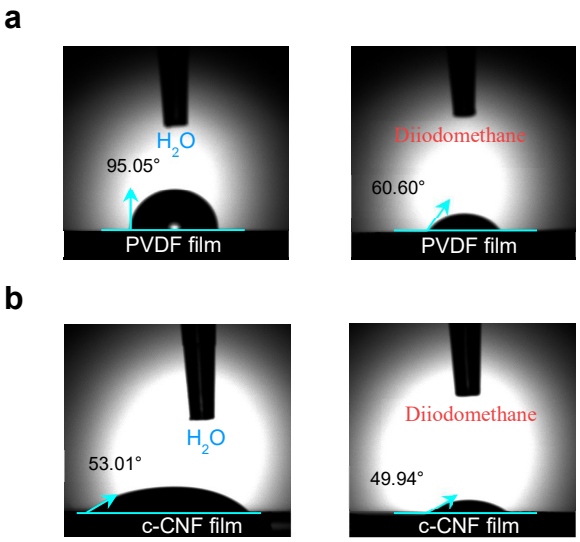

Supplementary Fig. 14 | Surface wettability and adhesion characteristics of binder films. a, Contact angles of H_2O and diiodomethane on the PVDF film. **b**, Contact angles of H_2O and diiodomethane on the c-CNF film. Surface energy components were calculated using the Owens–Wendt method, where γ_s^d and γ_l^d represent the dispersive components, and γ_s^p and γ_l^p denote the polar components of the surface energy for the solid (s) and liquid (l), respectively. θ represents the measured contact angle. The work of adhesion (W_a) was estimated using the following equation[4]:

$$\left(\gamma_s^d \gamma_l^d\right)^{0.5} + \left(\gamma_s^p \gamma_l^p\right)^{0.5} = 0.5\gamma_l(1+\cos\theta) \quad (3)$$

$$W_a = 2\left(\gamma_s^d \gamma_l^d\right)^{0.5} + 2\left(\gamma_s^p \gamma_l^p\right)^{0.5} \quad (4)$$

Material	Contact angle [H_2O]	Contact angle [Diiodomethane]	γ^d	γ^p	γ^{total}
PVDF	95.05°	60.60°	28.16	1.63	29.79
c-CNF	53.01°	49.94°	34.32	19.13	53.45

Material	Work of cohesion	
	PVDF	c-CNF
PVDF	59.58	
c-CNF		106.9

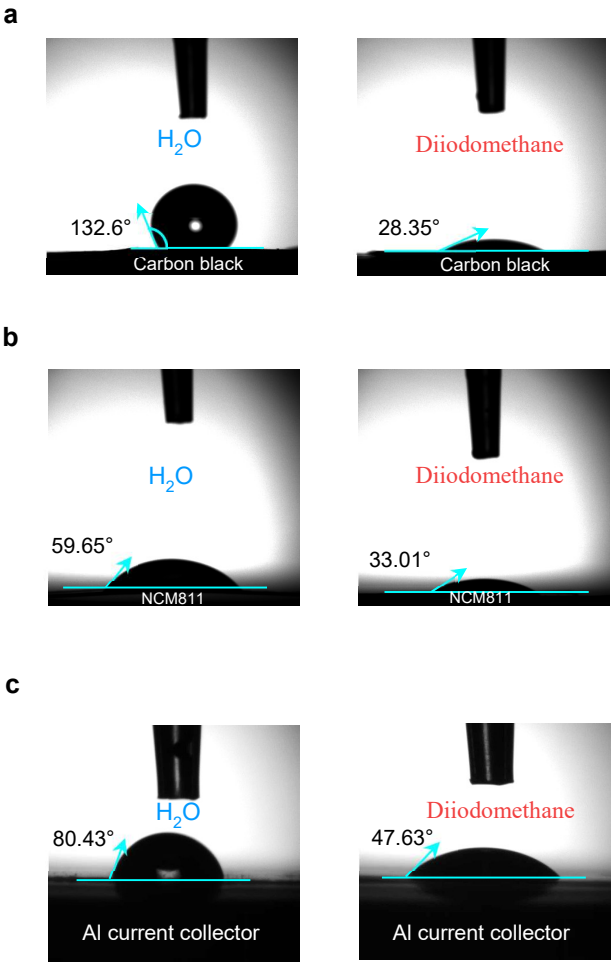

Supplementary Fig. 15 | Surface wettability of individual electrode components. Contact angles of H_2O and diiodomethane measured on carbon black film (**a**), NCM811 film (**b**), and Al current collector (**c**), respectively, to evaluate their surface energy characteristics.

Material	Contact angle (H_2O)	Contact angle (Diiodomethane)	γ^d	γ^p	γ^{total}
Carbon black	132.6°	28.35°	44.89	6.38	51.27
NCM811	59.65°	33.01°	42.96	11.96	54.92
Al current collector	80.43°	47.63°	36.62	4.52	40.14

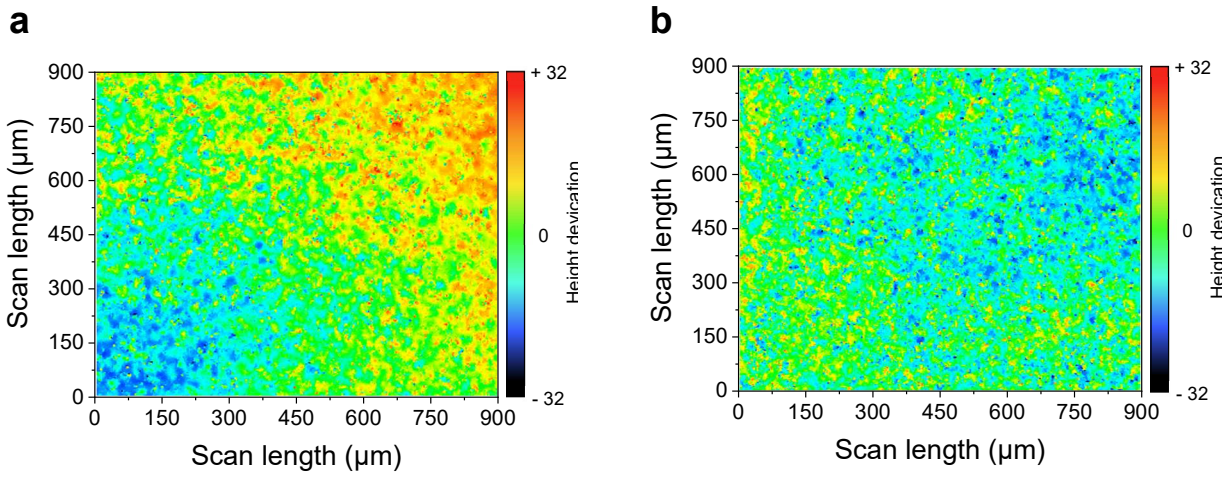

Supplementary Fig. 16 | Surface topography of electrodes analyzed by laser scanning confocal microscopy (LSCM). a, PVDF electrode. **b**, c-CNF electrode. Topographic images were obtained at a high areal mass loading ($M/A = 40$ mg cm^{-2}) to evaluate surface uniformity and calendering tolerance.

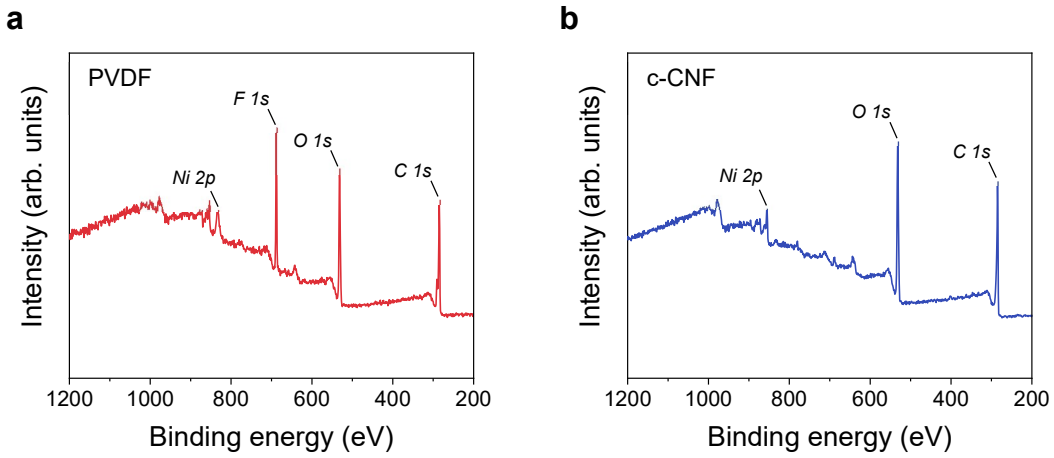

Supplementary Fig. 17 | XPS analysis of electrodes. a, Full scan XPS spectrum of PVDF electrode. **b**, Full scan XPS spectrum of c-CNF electrode. The elemental composition and surface chemistry differences between the two binder systems are revealed through survey spectra.

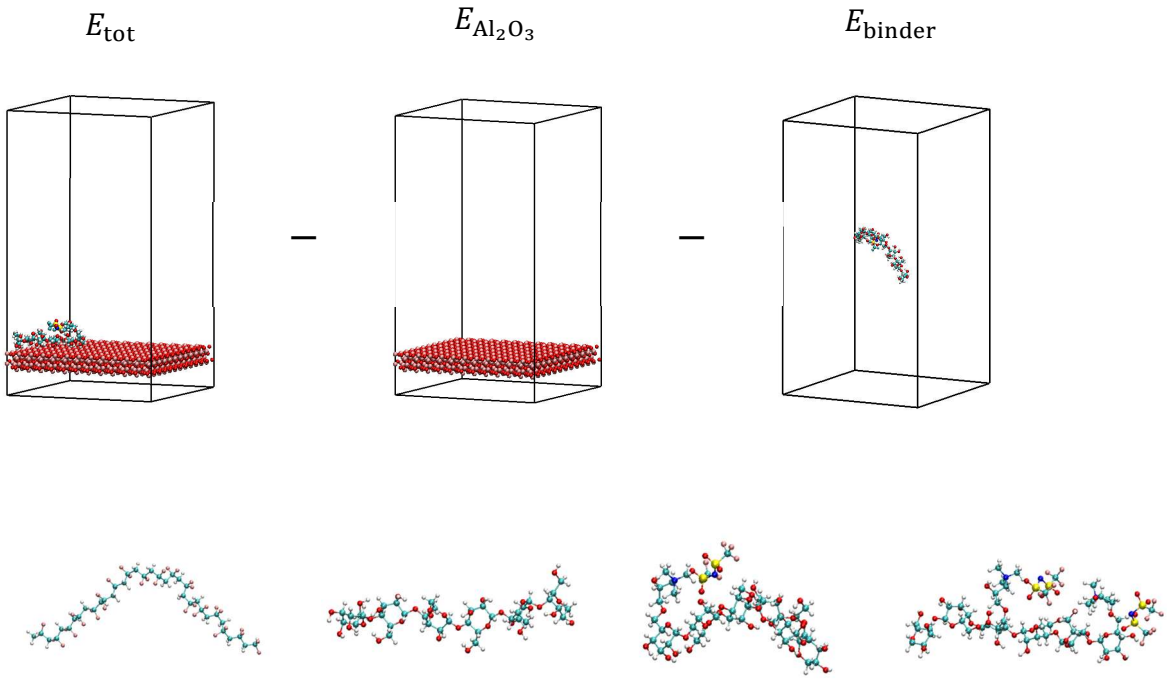

	PVDF	CNF (6 repeat unit)	1 c-CNF (one cationic group)	2 c-CNF (two cationic group)
Mass	1154.628	974.832	1091.015	1207.198
ΔE [kJ/mol]	-530.26	-1060.87	-1204.8	-1193.79

Supplementary Fig. 18 | MD-calculated binding energies between binder materials (PVDF, b-CNF, and c-CNF) and Al current collector. The Al_2O_3 layer represents the native oxide surface of the Al current collector. The model highlights the critical role of binder functional groups in determining interfacial adhesion. Stabilization energies were calculated using equation[5]:

$$E_{tot} - E_{Al_2O_3} - E_{binder} \quad (5)$$

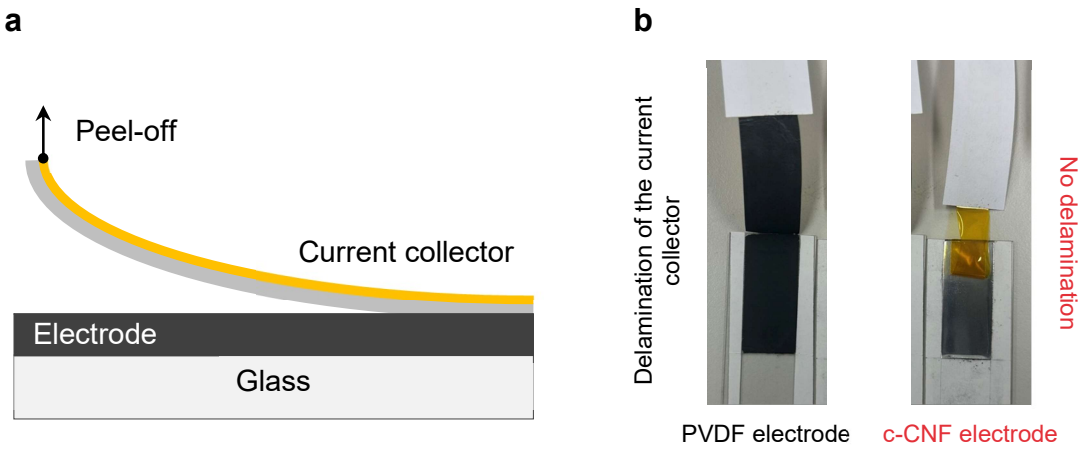

Supplementary Fig. 19 | Adhesion evaluation via 180° peel-off test. a, Schematic illustration of the 180° peel-off test performed between the current collector and electrode layers. **b**, Photographs of electrodes after the peel-off test (PVDF electrode vs. c-CNF electrode), highlighting differences in interfacial adhesion.

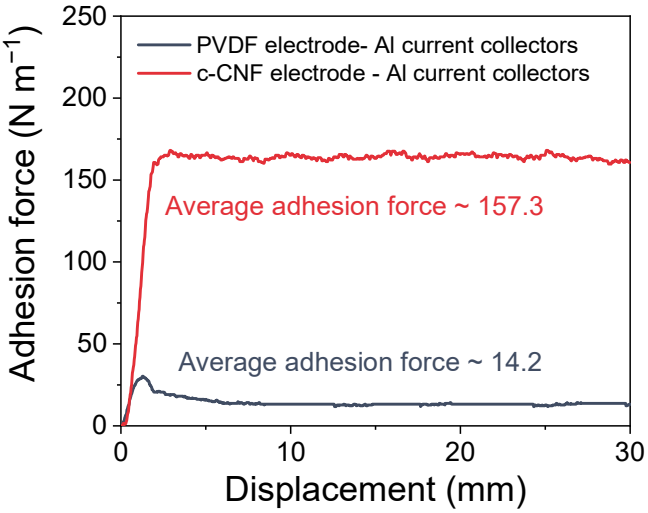

Supplementary Fig. 20 | Quantitative adhesion force measured by 180° peel-off test. Adhesion force between the current collector and electrode layers (PVDF vs. c-CNF), highlighting the enhanced interfacial strength of the c-CNF electrode.

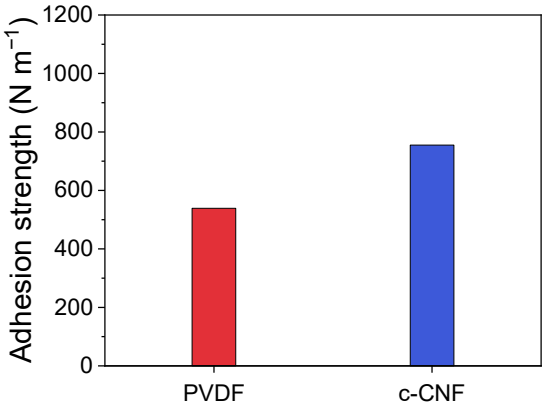

Supplementary Fig. 21 | Adhesion strength measured by SAICAS. Interfacial adhesion between the current collector and electrode layers for PVDF and c-CNF systems is compared.

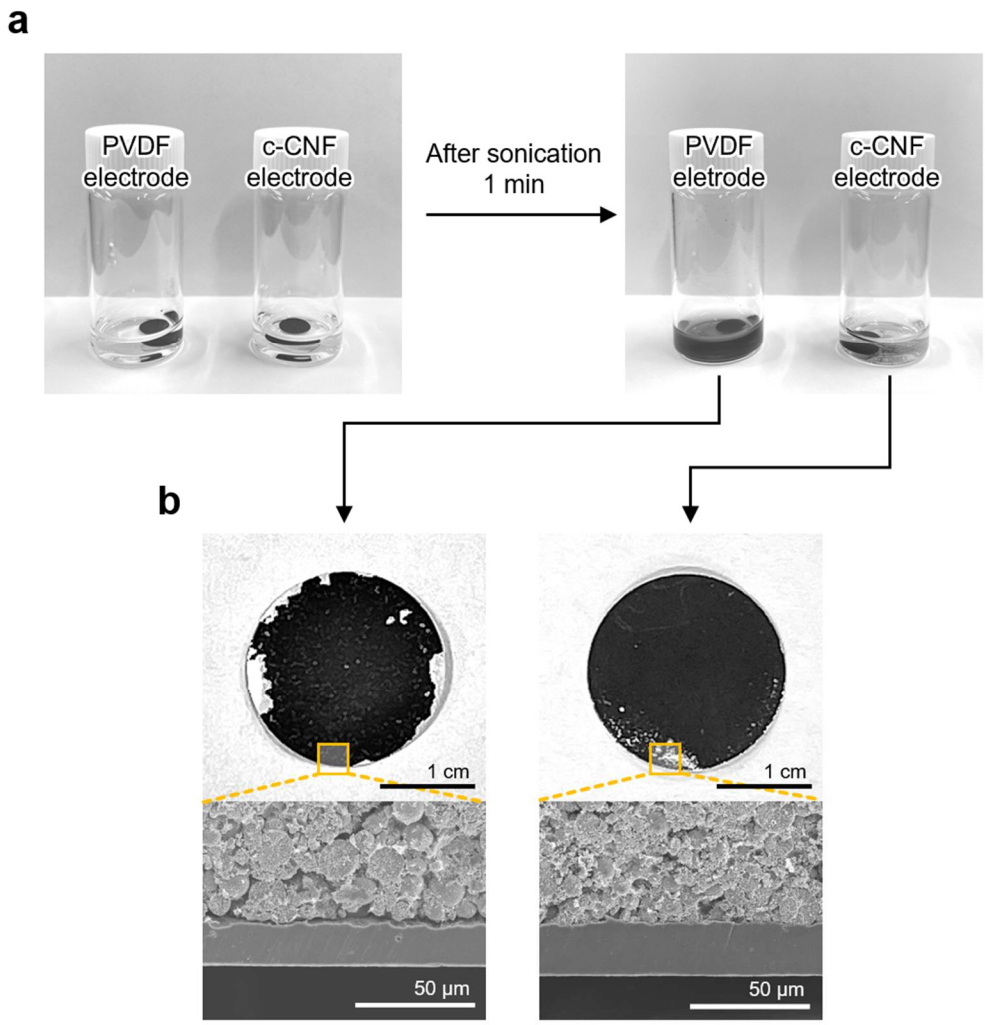

Supplementary Fig. 22 | Mechanical integrity of PVDF– and c-CNF–based electrodes after electrolyte immersion. a, Photographs of electrodes immersed in a liquid electrolyte (1 M $LiPF_6$ in EC/EMC (3/7, v/v)): (left) before and (right) after 1 min sonication applied as an external stress to accelerate structural failure. **b**, Photographs and cross-sectional SEM images of the electrodes after the treatment.

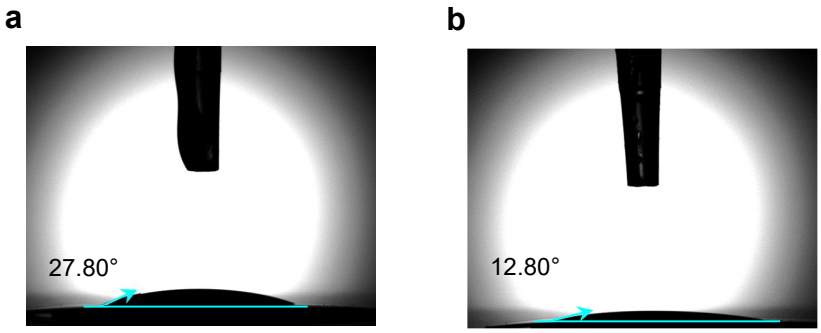

Supplementary Fig. 23 | Contact angles of liquid electrolyte on PVDF and c-CNF electrodes. PVDF (a) and c-CNF (b) electrodes are compared.

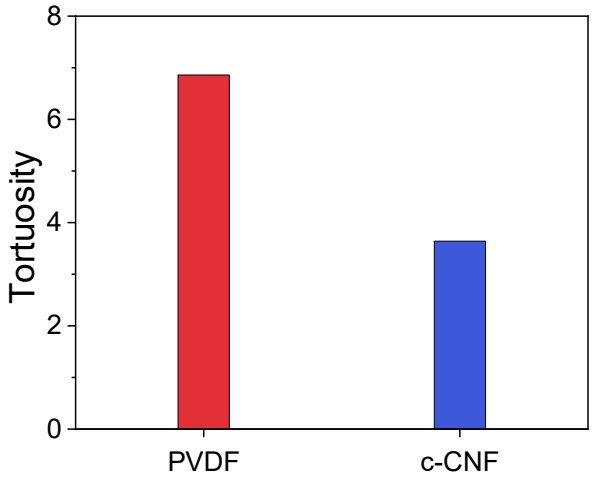

Supplementary Fig. 24 | Calculated tortuosity of c-CNF and PVDF electrodes. Tortuosity (τ) values were calculated using the following equation[6]:

$$\tau = \frac{R_{ion}\, A\, k\, \varepsilon}{2d} \quad (6)$$

where R_{ion}, A, k, ε, and d represent the ion transport resistance, the surface area of the electrode, the conductivity of the electrolyte, the porosity, and the thickness of the electrode, respectively.

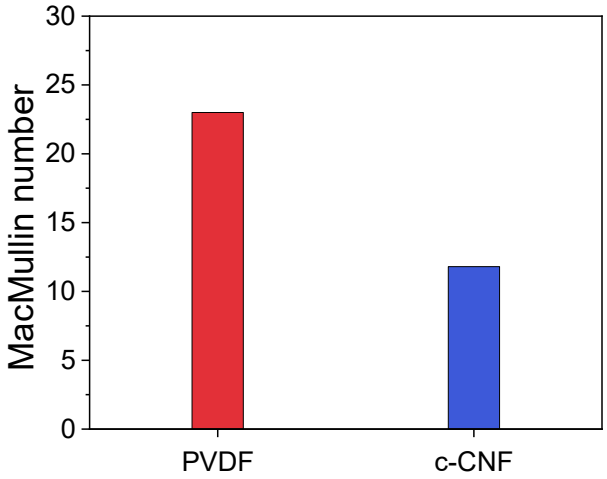

Supplementary Fig. 25 | MacMullin number of c-CNF and PVDF electrodes. The effective ion diffusion characteristics were evaluated by calculating the MacMullin number (N_M) using the following equation[7]:

$$N_M = \frac{K_{bulk}}{K_{eff}} = \frac{\tau}{\varepsilon} \quad (7)$$

where K_{eff}, K_{bulk}, τ, and ε represent the effective ionic conductivity in the pores of the electrode, bulk ionic conductivity of the electrolyte, tortuosity, and porosity, respectively.

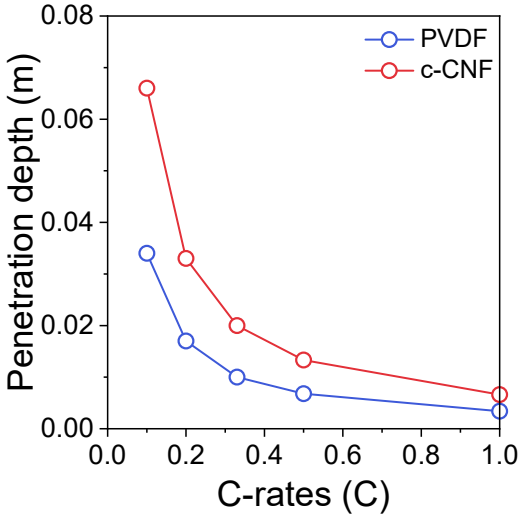

Supplementary Fig. 26 | Calculated penetration depth of lithium ions in c-CNF and PVDF electrodes. The ion penetration depth (L_d) was estimated using the following equation[8]:

$$L_{\mathrm{d}} = \frac{\varepsilon}{\tau}\frac{D_0 C_0 F}{(1-t_{\mathrm{Li+}})I} \quad (8)$$

where ε is the electrode porosity, τ is the tortuosity, D_0 is the diffusion coefficient of the lithium salt in the electrolyte, C_0 is the initial electrolyte concentration, F is the Faraday constant, $t_{\mathrm{Li+}}$ is the Li^+ transference number, and I is the applied current density.

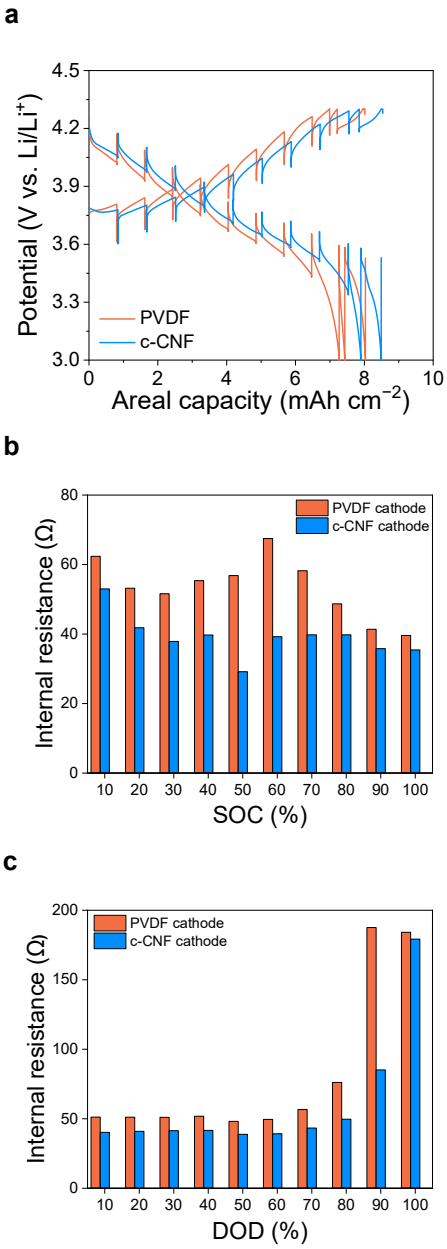

Supplementary Fig. 27 | Electrochemical analysis of c-CNF and PVDF electrodes via GITT. a, GITT profiles obtained upon repeated current pulses at a current density of 0.5 C, with a 1 h rest period between the pulses. **b**, Internal resistance as a function of SOC. **c**, Internal resistance as a function of DOD.

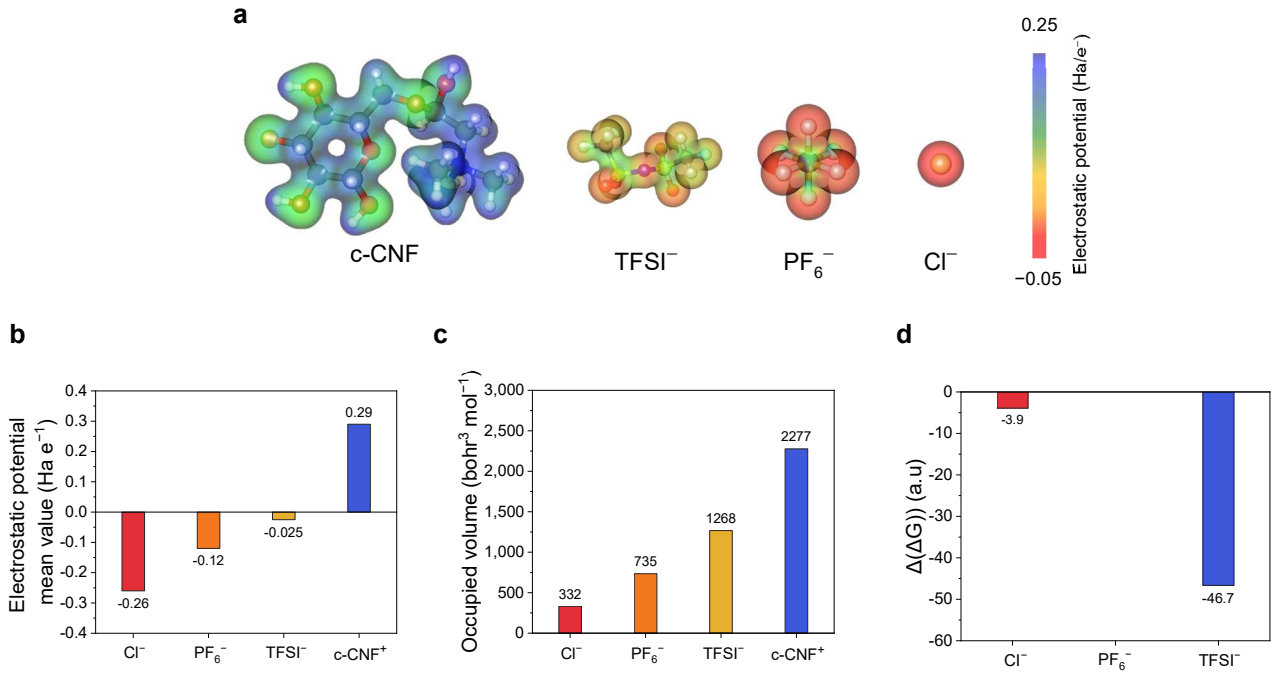

Supplementary Fig. 28 | Molecular interactions between c-CNF and various counter anions. a, Electrostatic potential maps of c-CNF and counter anions (Cl^-, PF_6^-, and $TFSI^-$), where red and blue indicate electron-rich and electron-deficient regions, respectively. **b**, Comparison of the mean molecular electrostatic potential (MEP) values of the anions. **c,** Comparison of occupied volumes of the anions and c-CNF. **d**, Free energy of each c-CNF–anion pair, illustrating the relative binding affinity of Cl^-, PF_6^-, and $TFSI^-$.

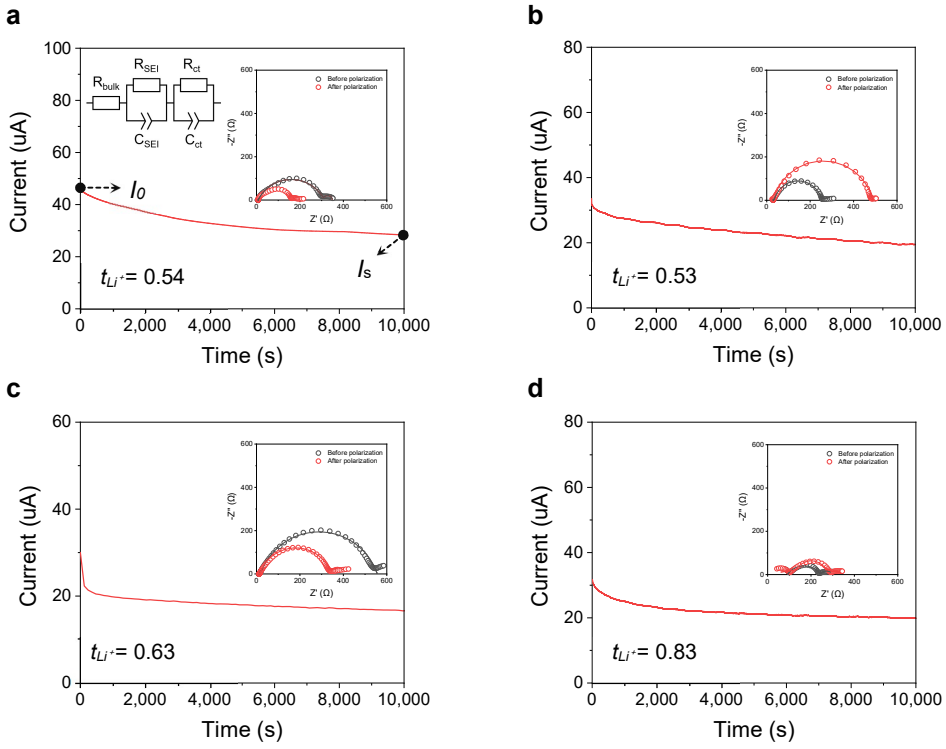

Supplementary Fig. 29 | Electrochemical impedance and current response of Li||Li symmetric cells. a–d, EIS spectra and corresponding time-dependent current profiles measured at 10 mV polarization, used for the determination of Li^+ transference number (t_{Li^+}) based on the Bruce–Vincent–Evans method. PVDF (**a**), b-CNF (**b**), c-CNF–Cl (**c**), and c-CNF–TFSI films (**d**), where symbols and solid lines represent the experimental data and fitted curves, respectively.

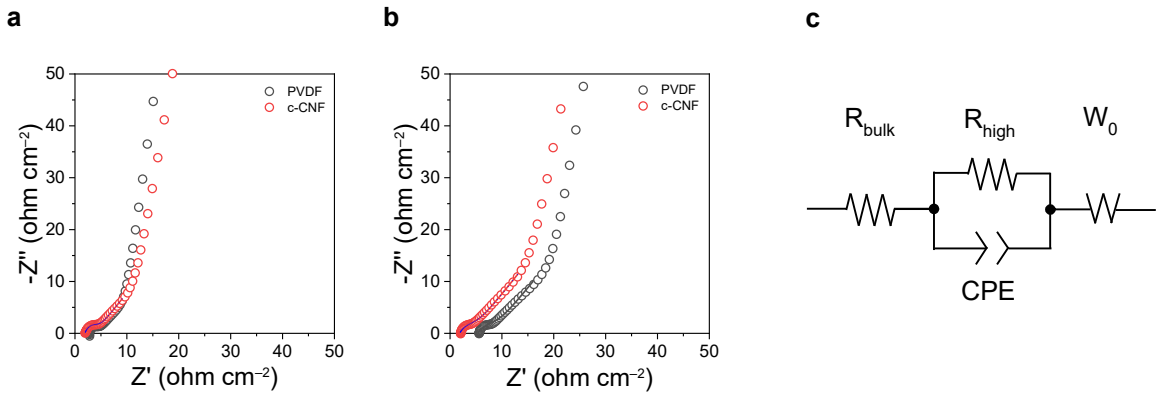

Supplementary Fig. 30 | Electrochemical impedance spectra of electrodes with various areal mass loadings. a, Nyquist plot of electrodes with an areal mass loading of 20 mg cm^{-2}, measured in a symmetric cell configuration at 0% SOC. **b**, Nyquist plot of electrodes with an areal mass loading of 30 mg cm^{-2} under the same conditions. **c**, Equivalent circuits using the generalized finite length Warburg element with open circuit terminus (W_0).

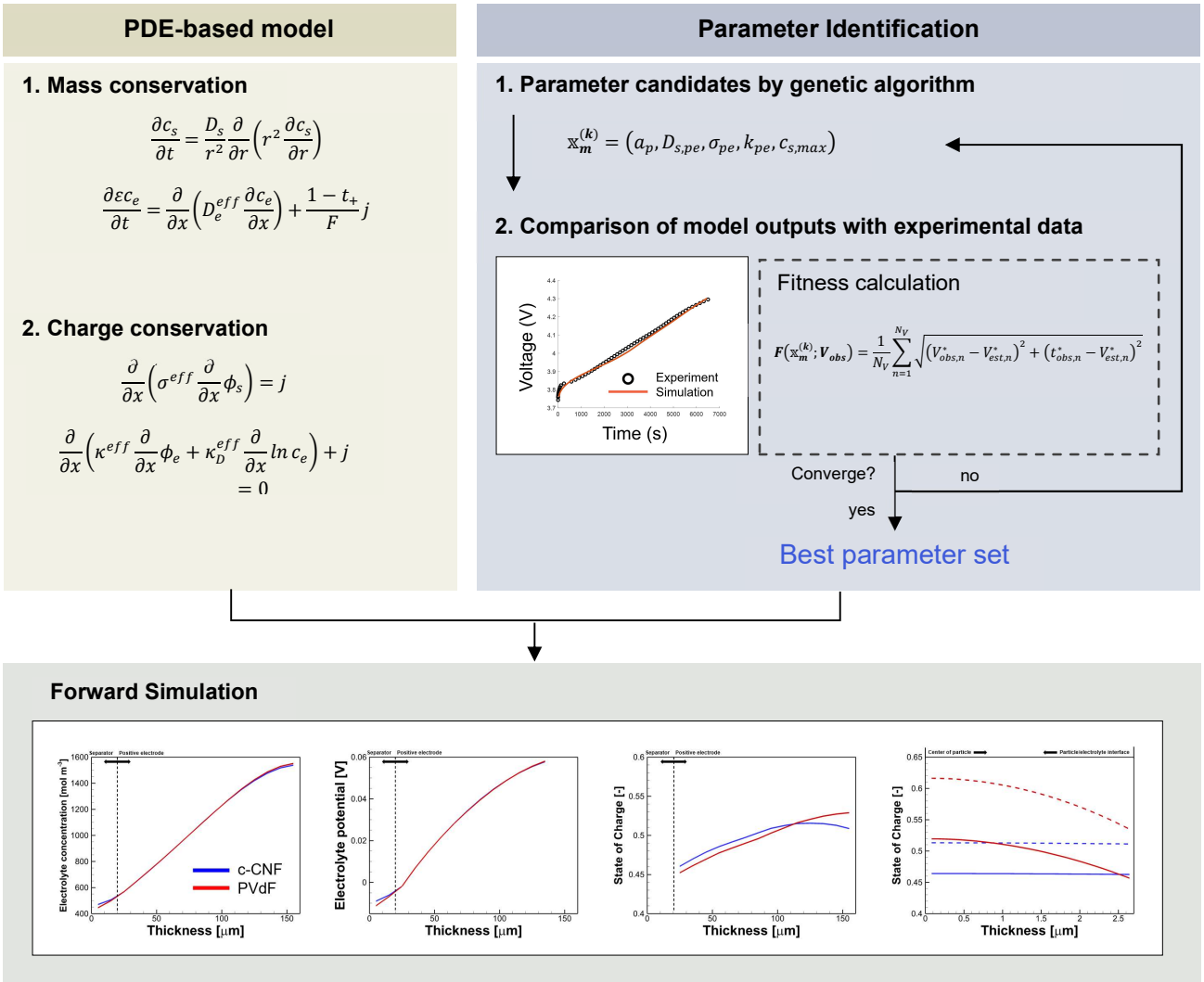

Supplementary Fig. 31 | Schematic overview of the PDE-based modeling and simulation workflow. The diagram illustrates the computational process used to simulate electrode behavior, including parameter identification and forward prediction based on experimentally informed PDE models.

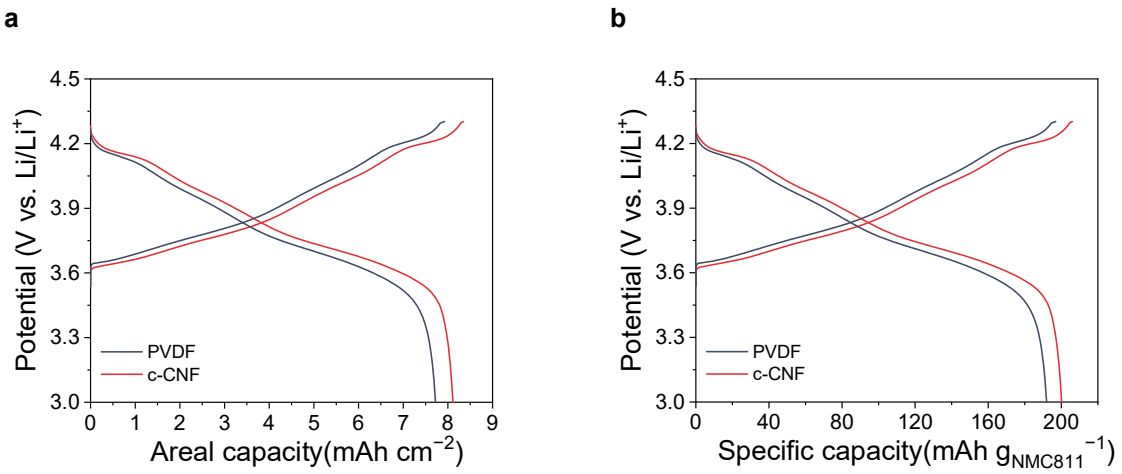

Supplementary Fig. 32 | Galvanostatic charge/discharge profiles of Li-metal cells with an areal mass loading of 40 mg cm^{-2}. The profiles are plotted as a function of specific capacity (**a**) and areal capacity (**b**).

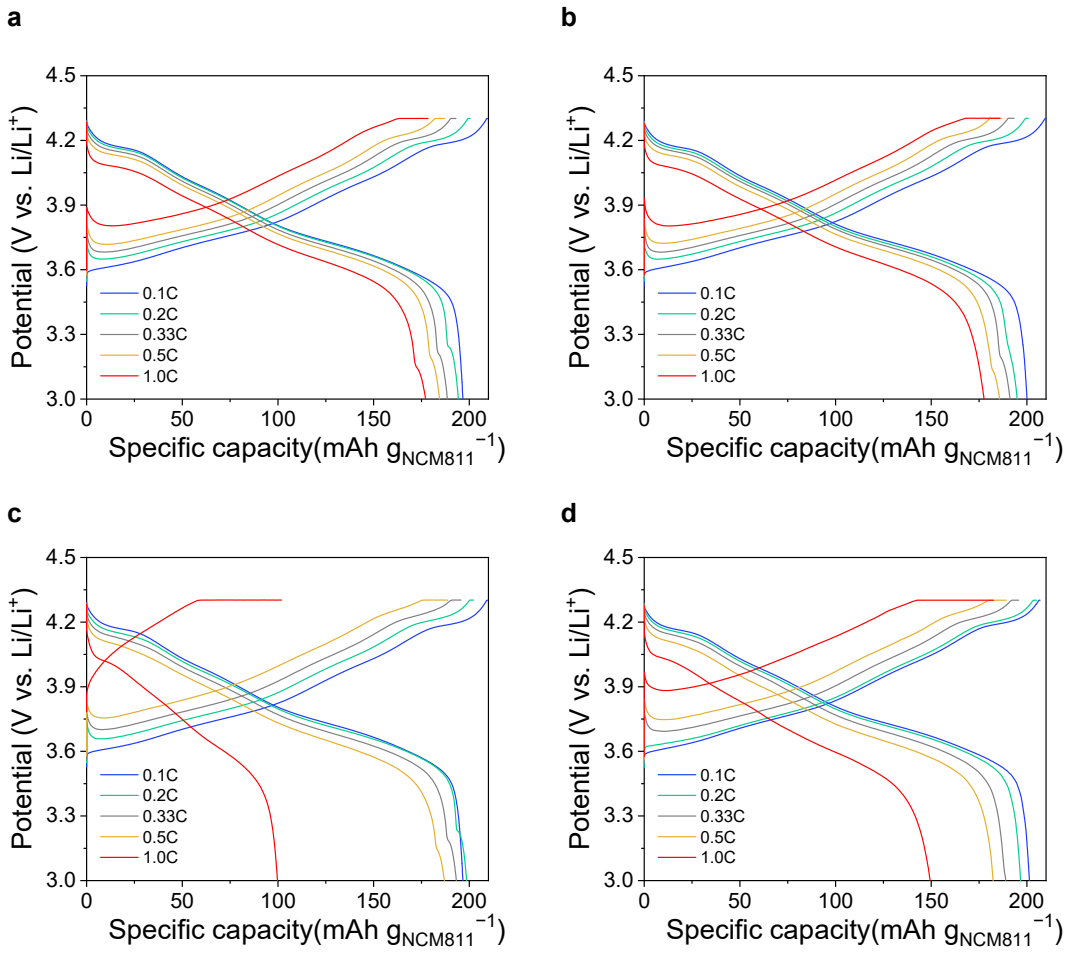

Supplementary Fig. 33 | Galvanostatic charge/discharge profiles. a, PVDF electrodes at an areal mass loading of 20 mg cm^{-2}. **b**, c-CNF electrodes at 20 mg cm^{-2}. **c**, PVDF electrodes at 30 mg cm^{-2}. **d**, c-CNF electrodes at 30 mg cm^{-2}. All cells were tested under varied charge/discharge current rates to evaluate rate capability.

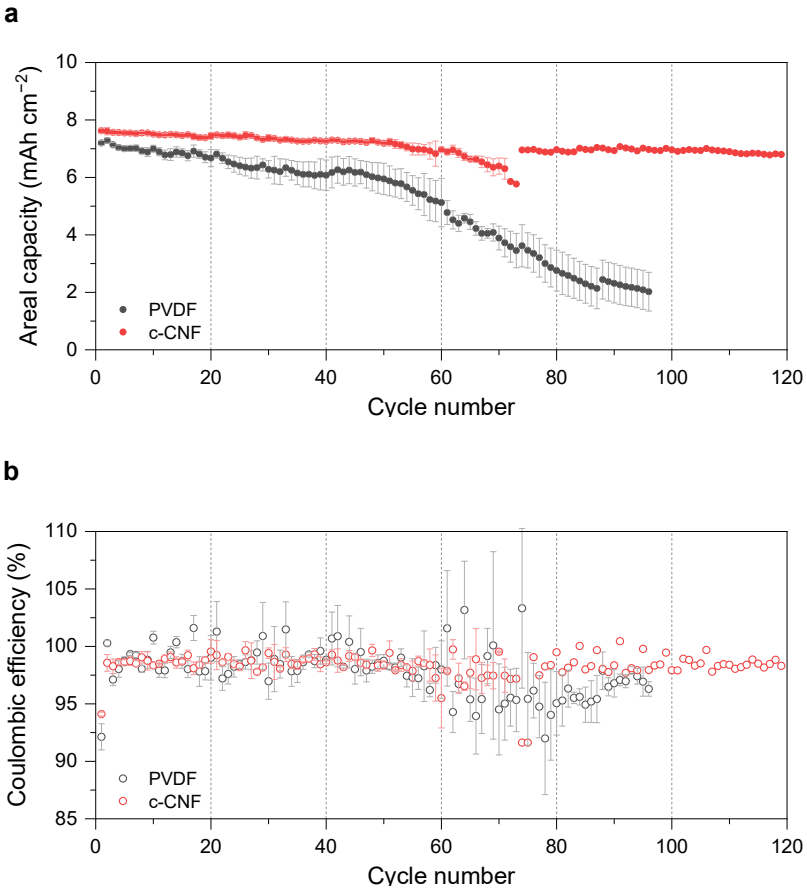

Supplementary Fig. 34 | Cycling behavior of PVDF and c-CNF electrodes. Areal capacity (**a**) and Coulombic efficiency (**b**) measured at a current density of 0.33 C (= 2.67 mA cm^{-2}). Error bars represent standard deviation from three independently tested cells (n = 3).

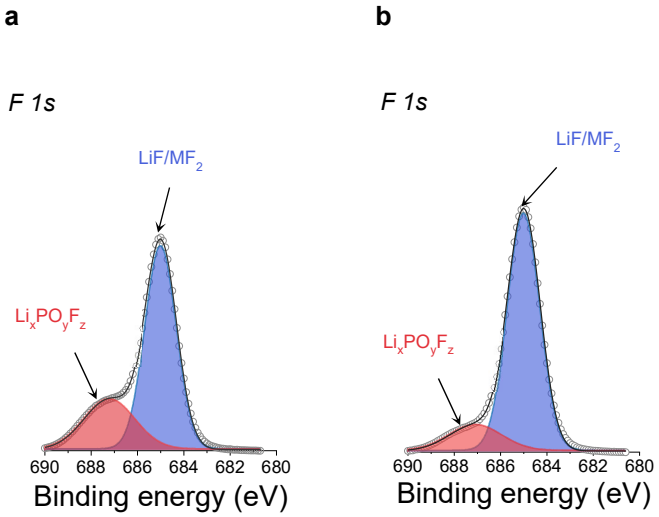

Supplementary Fig. 35 | F 1s XPS spectra of cycled electrodes. a, PVDF-based electrode. **b**, c-CNF-based electrode. Cells were cycled at 0.33 C (corresponding to 2.67 mA cm^{-2}) for 80 cycles within a voltage range of 3.0–4.3 V and were disassembled in the fully discharged state (corresponding to 0% state of charge) for ex situ analysis. The discharge areal capacity was approximately 8 mAh cm^{-2}. All electrochemical tests were conducted at 23 ± 1 °C.

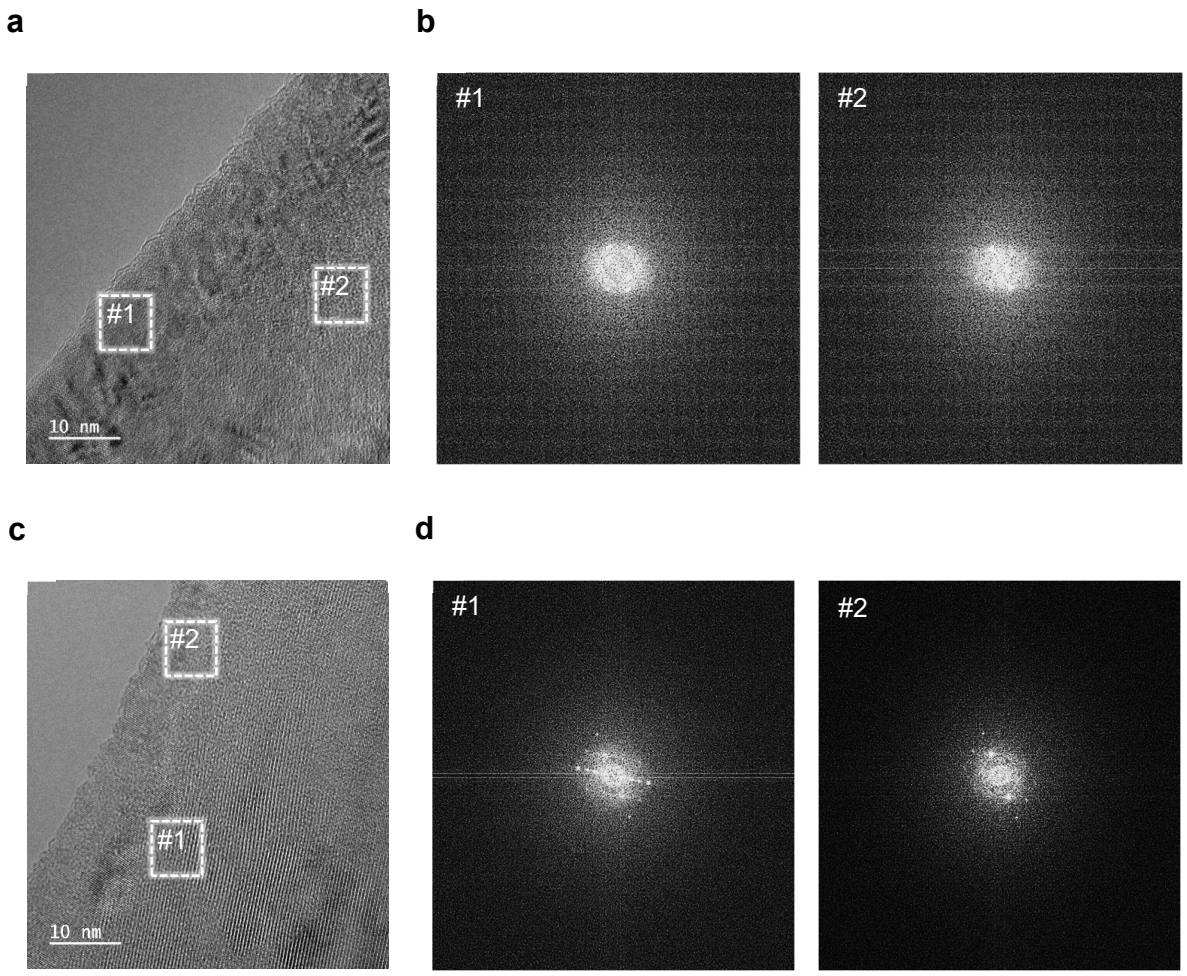

Supplementary Fig. 36 | HR-TEM and FFT analysis of cycled NCM811 particles. a, HR-TEM image of cycled NCM811 from the PVDF electrode. **b**, Corresponding FFT pattern of cycled NCM811 from the PVDF electrode. **c**, HR-TEM image of cycled NCM811 from the c-CNF electrode. **d**, Corresponding FFT pattern of cycled NCM811 from the c-CNF electrode. Cells were cycled at 0.33 C (corresponding to 2.67 mA cm^{-2}) for 80 cycles within a voltage range of 3.0–4.3 V and were disassembled in the fully discharged state (corresponding to 0% state of charge) for ex situ analysis. The discharge areal capacity was approximately 8 mAh cm^{-2}. All electrochemical tests were conducted at 23 ± 1 °C.

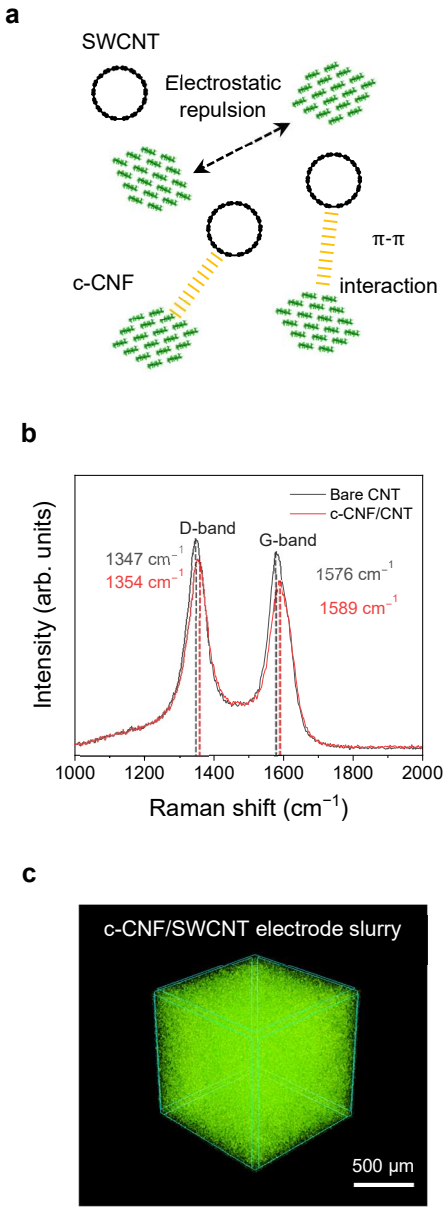

Supplementary Fig. 37 | Intermolecular interactions between c-CNF and SWCNT in electrode slurries. a, Schematic illustration of intermolecular interactions. The c-CNF binder facilitates stable dispersion by conformally interacting with SWCNT via noncovalent π–π interactions, while its cationic groups induce interparticle electrostatic repulsion. **b**, Raman spectra of c-CNF/SWCNT vs. pristine SWCNT. Both show characteristic D- and G-band peaks, with upshifts in the hybrid (D-band: 1347 → 1354 cm^{-1}; G-band: 1576 → 1589 cm^{-1}), indicating noncovalent interactions between c-CNF and SWCNT. **c**, Micro-CT image of c-CNF/SWCNT-based electrode slurry, revealing uniform dispersion and structural homogeneity.

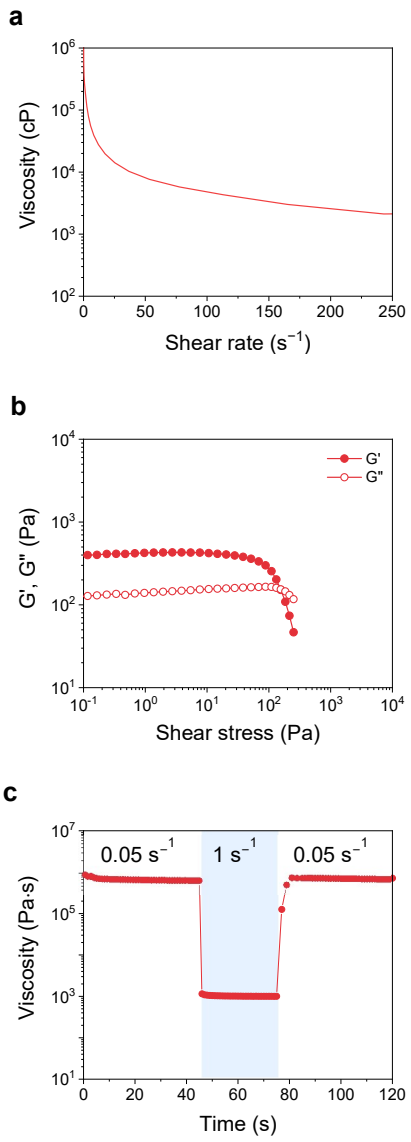

Supplementary Fig. 38 | Rheological characterization of c-CNF/SWCNT-based electrode slurries. **a**, Viscosity as a function of shear rate. **b**, Viscoelastic moduli (G′ and G″) as a function of shear stress. **c**, 3ITT profiles showing structural recovery of electrode slurries after shear-induced structural disruption (shear rate increased from 0.05 to 1 s^{-1}).

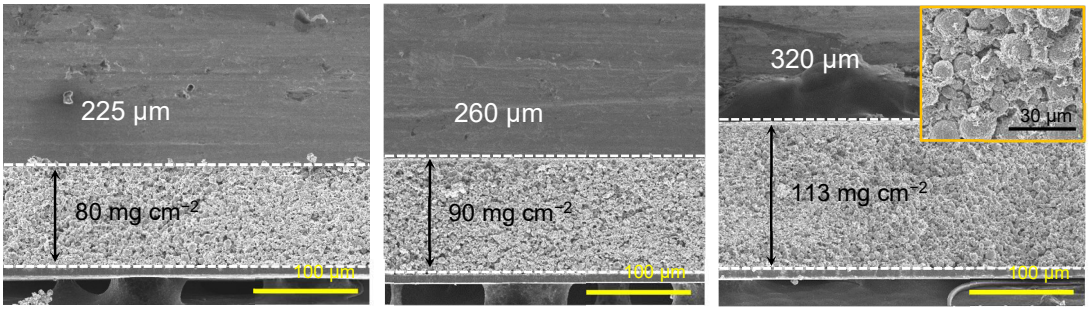

Supplementary Fig. 39 | Cross-sectional SEM images of c-CNF electrodes as a function of areal mass loading. Electrodes with different areal mass loadings were prepared under identical processing conditions to examine structural uniformity.

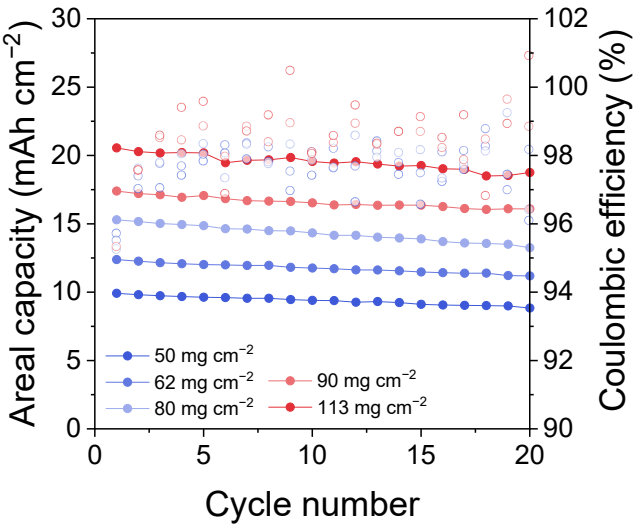

Supplementary Fig. 40 | Cycling performance as a function of areal mass loading. Measurements were conducted at charge/discharge rate of 0.1 C/0.1 C (1 C = 200 mA g^{-1}) within 3.0–4.3 V.

a

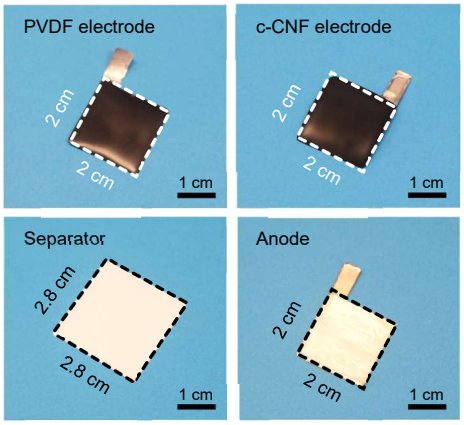

b

Components	Weight (mg)	Thickness (μm)
PVDF electrode	166.2	136
c-CNF electrode	370.7	336
Separator	7.85	16
Anode	111.5	109

c

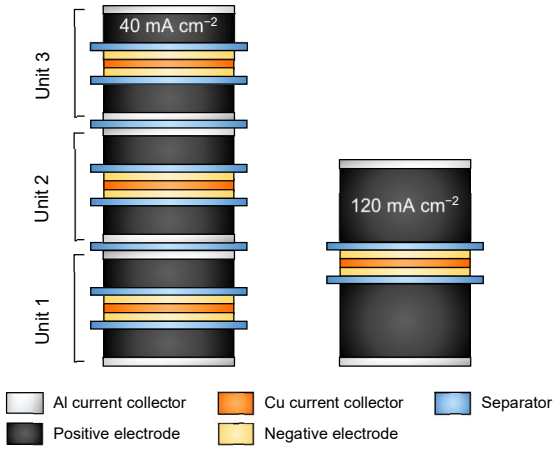

Supplementary Fig. 41 | Pouch cell configuration and component comparison between PVDF and c-CNF electrodes. a, Photographs of the pouch cell components, including PVDF electrode (40 mg cm^{-2}) or c-CNF electrode (120 mg cm^{-2}), PE separator, and Li-metal on a Cu current collector. **b**, Summary of component specifications for the pouch cells used in this study. **c**, Schematic illustration of multi-stack pouch cell configurations. Each unit cell is defined as a double-stacked structure. The PVDF-based pouch cell contains three unit cells, while the c-CNF-based pouch cell contains a single unit cell, with both designed to achieve identical total cell capacities (~0.44 Ah).

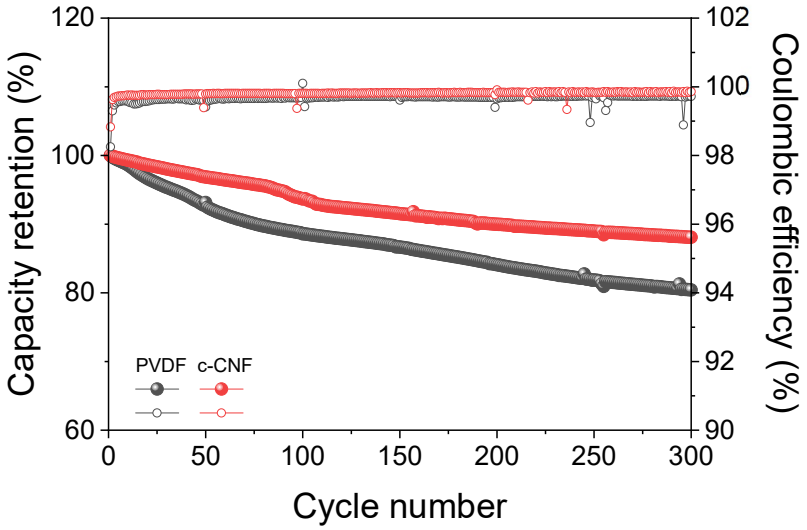

Supplementary Fig. 42 | Cycling performance of graphite (4.2 mAh cm^{-2})||NCM811 (4.0 mAh cm^{-2}; N/P = 1.05) full cells. Measurements were conducted at a charge/discharge current density of 1.32 mA cm^{-2}/1.32 mA cm^{-2} within a voltage range of 2.8–4.2 V.

Supplementary Tables

Supplementary Table 1 | Calculation details for work of adhesion values representing the chemical affinity between different materials.

Material	Work of adhesion (mN m^{-1})		
	Carbon black	NCM811	Al current collector
PVDF	77.56	78.40	68.77
c-CNF	103.6	107.1	88.53

Supplementary Table 2 | Parameters used for calculating the Li^+ transference number (t_{Li^+}) based on the Bruce–Vincent–Evans method. The initial (I_0) and steady-state (I_s) currents were obtained under an applied potential of 10 mV during potentiostatic polarization. The interfacial resistances before (R_0) and after (R_s) polarization were determined from electrochemical impedance spectroscopy (EIS), respectively.

Binder	Applied voltage (mV)	I_0 (mA)	I_s (mA)	R_0 (Ohm)	R_s (Ohm)	t_{Li^+}
PVDF	10	0.046	0.028	169.0	311.0	0.54
b-CNF	10	0.033	0.019	263.1	493.9	0.53
c-CNF–Cl	10	0.030	0.016	353.2	556.9	0.63
c-CNF–TFSI	10	0.031	0.019	251.7	304.9	0.83

Supplementary Table 3 | Fitted resistance components obtained from EIS for PVDF and c-CNF electrodes as a function of mass loading. The bulk resistance (R_{bulk}) and high-frequency interfacial resistance (R_{high}) were extracted from equivalent circuit fitting at loadings of 20, 30, and 40 mg cm^{-2}. The fitting quality is indicated by χ^2 and the normalized error ($\chi^2/|Z|^2$).

Sample	Loading (mg cm^{-2})	R_{bulk}	R_{high}	χ^2	$\chi^2/\|Z\|^2$
PVDF	20	2.72	1.56	1.53	0.16
	30	5.31	3.08	1.69	0.03
	40	2.81	36.56	3.25	0.12
c-CNF	20	1.88	2.03	0.22	0.02
	30	1.82	2.42	1.09	0.09
	40	2.53	9.84	1.46	0.08

Supplementary Table 4 | Calculation details for the specific energy densities of cells containing high-density (ρ = 3.65 g cm^{-3}) c-CNF electrodes.

Binder	Mass loading [mg cm^{-2}]	Areal capacity [mAh cm^{-2}]	Capacity [mAh]	Nominal voltage [V]	$M_{positive}$ [mg]	$M_{negative}$ [mg]	$M_{separator}$ [mg]	$M_{electrolyte}$ [mg]	M_{total} [mg]	Specific energy [Wh kg^{-1}]
PVDF	40	7.7	6.04	3.65	39.25	14.90	2.49	12.09	68.73	320.9
c-CNF	40	8.0	6.28	3.65	39.25	14.90	2.49	12.56	69.20	331.1
c-CNF	50	10.0	7.85	3.65	47.10	14.90	2.49	15.70	80.19	357.2
c-CNF	62	12.6	9.89	3.65	56.52	14.90	2.49	19.78	93.69	385.2
c-CNF	80	15.9	12.48	3.65	70.65	14.90	2.49	24.96	113.00	403.1
c-CNF	90	18.0	14.13	3.65	78.50	14.90	2.49	28.26	124.15	415.3
c-CNF	113	22.5	17.66	3.65	96.56	14.90	2.49	35.33	149.28	431.8

The specific energy of the cell was calculated using the following equation[9,10]:

$$(9) \qquad Specific\ energy\ (\text{Wh kg}^{-1}) = \frac{Energy}{Mass\ of\ cell} = \frac{Nominal\ voltage\ x\ C}{M_{positive}+M_{negative}+M_{separator}+M_{electrolyte}}$$

where the $M_{positive}$, $M_{negative}$, $M_{separator}$, and $M_{electrolyte}$ represent the mass of positive electrode (including Al current collector), negative electrode (including Cu current collector), separator, and electrolyte, respectively. C denotes the discharge capacity. The cells were fabricated using positive electrodes with various areal capacities (C/A) values and 100 μm-thick Li-metal negative electrodes (corresponding to 20 mAh cm^{-2}). The electrolyte mass/cell capacity (E/C) ratio in the cell was assumed to be 2.0 g Ah^{-1}. The mass values for the anode, separator, and electrolyte were estimated based on assumptions commonly used in cell-level analysis[11,12].

Supplementary Table 5 | Calculation details for the volumetric energy densities of cells containing high-density (ρ = 3.65 g cm^{-3}) c-CNF electrodes, where $T_{positive}$, $T_{negative}$, $T_{separator}$ are the thickness of positive electrode (including 16 μm of Al current collector), negative electrode (including 9 μm of Cu current collector), and separator, respectively.

Binder	C/A [mAh cm^{-2}]	Nominal voltage [V]	$T_{positive}$ [μm]	$T_{negative}$ [μm]	$T_{separator}$ [μm]	Energy density [Wh L^{-1}]
PVDF	7.7	3.65	136	109	16	1076.8
c-CNF	8.0	3.65	127	109	16	1158.7
c-CNF	10.0	3.65	159	109	16	1285.2
c-CNF	12.6	3.65	191	109	16	1455.7
c-CNF	15.9	3.65	241	109	16	1586.3
c-CNF	18.0	3.65	276	109	16	1638.4
c-CNF	22.5	3.65	336	109	16	1781.5

The volumetric energy density of the cell was calculated using the following equation[10]:

(10) $$Energy\ density\ (Wh\ L^{-1}) = \frac{Energy}{Volume\ of\ cell} = \frac{Nominal\ voltage\ x\ C/A}{T_{\mathrm{positive}} + T_{\mathrm{negative}} + T_{\mathrm{separator}}}$$

Supplementary Table 6 | Comparison of positive electrode composition, areal capacity, and electrode density between this work and previously reported binder systems.

*AM: Active materials
C: Conductive agents
B: Binder

Materials	Active materials	Composition *[AM:C:B]	Areal mass loading [mg cm^{-2}]	Areal capacity [mAh cm^{-2}]	Electrode density [g cm^{-3}]	Cell energy density (Wh L^{-1})	Reference
c-CNF	NCM811	98.5:0.5:1.0	113	22.5	3.65	1781.5	This work
c-IPN	NCM811	92:3:5	96	20	2.9	1430.2	10
Bottlebrush PAA (BBP)	NCM811	97:2:1	27	5.2	2.9	895.9	11
PNCL	NCM811	90:5:5	22	4.5	2.4	818.7	12
Spandex	NCM811	94:4:2	16	3.2	2.4	609.6	13
CMC/PAA	NCM811	95.5/2/2.5	50	10	3.0	1489.8	14
Gel-electrolyte	NCM811	75/5/20	60	12.3	2.5	1020.3	15
Cellulose/CNT	LCO	80/6.7/13.3	90	12.1	2.5	768.1	16

Supplementary Table 7 | Cost comparison of binder materials and processing solvents used in this study.

	Material	Specific cost [USD g^{-1}]
PVDF binder	PVDF	1.20
	NMP	0.092
	Total	2.64
c-CNF binder	Cellulose nanofibrils (CNF)	0.386
	(3-Chloro-2-hydroxypropyl)trimethyl ammonium chloride	0.119
	Urea	0.055
	Sodium hydroxide	0.099
	Ethylene glycol	0.061
	Total	1.59

The unit costs for PVDF and NMP were taken from commercial quotations and market prices, whereas those for c-CNF and the processing solvents were estimated from a bottom-up bill-of-materials calculation using the experimental yield (USD g^{-1}). The total cost was calculated based on the actual composition of each binder system used in the slurry, weighted by the mass fraction of each component.

Supplementary Table 8 | **a**, Green scores of NMP and EG, the processing solvents used for PVDF and c-CNF electrodes, respectively, based on the GlaxoSmithKline (GSK) solvent selection guide[17,18]. Legislative concerns are flagged where applicable. **b**, Green scores of c-CNF and PVDF binder materials, evaluated according to environmental, health, and safety (EHS) criteria[19].

a

Electrode	Solvent	Environmental impact	Health	Life cycle assessment	Waste	Flag	Green score (0~40)
PVDF	NMP	6	3	4	5	*	18
c-CNF	EG	8	7	8	6	−	29

b

Electrode	Binder	PFAS-free	Sustainability	Synthesis	Biodegradability	Green score (−4 ~ +4)
PVDF	PVDF	−	−	−	−	-4
c-CNF	CNF	+	+	+	+	+4

Supplementary Reference

1 Zhang, H. *et al.* Homogeneous synthesis and characterization of polyacrylamide-grafted cationic cellulose flocculants. *Journal of Applied Polymer Science* **133** (2016).

2 Li, Z. *et al.* Sustainable high-strength macrofibres extracted from natural bamboo. *Nature Sustainability* **5**, 235-244 (2022).

3 M'barki, A., Bocquet, L. & Stevenson, A. Linking rheology and printability for dense and strong ceramics by direct ink writing. *Scientific reports* **7**, 6017 (2017).

4 Żenkiewicz, M. Methods for the calculation of surface free energy of solids. *Journal of Achievements in Materials and Manufacturing Engineering* **24**, 137-145 (2007).

5 Yao, X. *et al.* In situ interweaved high sulfur loading Li–S cathode by catalytically active metalloporphyrin based organic polymer binders. *Advanced Materials* **35**, 2208846 (2023).

6 Landesfeind, J., Hattendorff, J., Ehrl, A., Wall, W. A. & Gasteiger, H. A. Tortuosity determination of battery electrodes and separators by impedance spectroscopy. *Journal of The Electrochemical Society* **163**, A1373 (2016).

7 Yan, Z., Wang, L., Zhang, H. & He, X. Determination and Engineering of Li-Ion Tortuosity in Electrode Toward High Performance of Li-Ion Batteries. *Advanced Energy Materials* **14**, 2303206 (2024).

8 Tambio, S. *et al.* The concept of effective porosity in the discharge rate performance of high-density positive electrodes for automotive application. *Journal of The Electrochemical Society* **167**, 160509 (2020).

9 Hong, Y.-K. *et al.* Cellulose Elementary Fibrils as Deagglomerated Binder for High-Mass-Loading Lithium Battery Electrodes. *Nano-Micro Letters* **17**, 112 (2025).

10 Kim, J.-H. *et al.* Regulating electrostatic phenomena by cationic polymer binder for scalable high-areal-capacity Li battery electrodes. *Nature communications* **14**, 5721 (2023).

11 Kim, N. Y. *et al.* Amphiphilic bottlebrush polymeric binders for high-mass-loading cathodes in lithium-ion batteries. *Advanced Energy Materials* **12**, 2102109 (2022).

12 Jeong, D., Kwon, D. S., Kim, H. J. & Shim, J. Striking a Balance: Exploring Optimal Functionalities and Composition of Highly Adhesive and Dispersing Binders for High-Nickel Cathodes in Lithium-Ion Batteries. *Advanced Energy Materials* **13**, 2302845 (2023).

13 Chang, B. *et al.* Highly elastic binder for improved cyclability of nickel-rich layered cathode materials in lithium-ion batteries. *Advanced Energy Materials* **10**, 2001069 (2020).

14 Kim, J.-H. *et al.* Kosmotropic aqueous processing solution for green lithium battery cathode manufacturing. *Nature Communications* **16**, 1-12 (2025).

15 Kim, J.-H., Kim, J.-M., Cho, S.-K., Kim, N.-Y. & Lee, S.-Y. Redox-homogeneous, gel electrolyte-embedded high-mass-loading cathodes for high-energy lithium metal batteries. *Nature communications* **13**, 2541 (2022).

16 Wang, H. *et al.* A universal aqueous conductive binder for flexible electrodes. *Advanced Functional Materials* **31**, 2102284 (2021).

17 Henderson, R. K. *et al.* Expanding GSK's solvent selection guide–embedding sustainability into solvent selection starting at medicinal chemistry. *Green Chemistry* **13**, 854-862 (2011).

18 Byrne, F. P. *et al.* Tools and techniques for solvent selection: green solvent selection guides. *Sustainable chemical processes* **4**, 1-24 (2016).

19 Bresser, D., Buchholz, D., Moretti, A., Varzi, A. & Passerini, S. Alternative binders for sustainable electrochemical energy storage–the transition to aqueous electrode processing and bio-derived polymers. *Energy & Environmental Science* **11**, 3096-3127 (2018).